

## A NEW METHOD FOR CONSTRAINING MOLECULAR CLOUD THICKNESS: A STUDY OF TAURUS, PERSEUS AND OPHIUCHUS

LEI QIAN<sup>1\*</sup>, DI LI<sup>1 2 4†</sup>, STELLA OFFNER<sup>3‡</sup> AND ZHICHEN PAN<sup>1§</sup>

## ABSTRACT

The core velocity dispersion (CVD) is a potentially useful tool for studying the turbulent velocity field of molecular clouds. CVD is based on centroid velocities of dense gas clumps, thus is less prone to density fluctuation and reflects more directly the cloud velocity field. Prior work demonstrated that the Taurus molecular cloud CVD resembles the well-known Larson's linewidth-size relation of molecular clouds. In this work, we studied the dependence of the CVD on the line-of-sight thickness of molecular clouds, a quantity which cannot be measured by direct means. We produced a simple statistical model of cores within clouds and analyzed the CVD of a variety of hydrodynamical simulations. We show that the relation between the CVD and the 2D projected separation of cores ( $L_{2D}$ ) is sensitive to the cloud thickness. When the cloud is thin, the index of **CVD- $L_{2D}$  relation** ( $\gamma$  in the relation  $\text{CVD} \sim L_{2D}^\gamma$ ) reflects the underlying energy spectrum ( $E(k) \sim k^{-\beta}$ ) in that  $\gamma \sim (\beta - 1)/2$ . The CVD- $L_{2D}$  relation becomes flatter ( $\gamma \rightarrow 0$ ) for thicker clouds. We used this result to constrain the thicknesses of Taurus, Perseus, and Ophiuchus. We conclude that Taurus has a ratio of cloud depth to cloud length smaller than about 1/10-1/8, i.e. it is a sheet. A simple geometric model fit to the linewidth-size relation indicates that the Taurus cloud has a  $\sim 0.7$  pc line-of-sight dimension. In contrast, Perseus and Ophiuchus are thicker and have ratios of cloud depth to cloud length larger than about 1/10-1/8.

*Keywords:* ISM: clouds — ISM: molecules

## 1. INTRODUCTION

Stars form in molecular clouds. There is much evidence that molecular clouds are turbulent, e.g. the observed molecular linewidth is much larger than the thermal linewidth. Because the interstellar medium (ISM) is turbulent, its velocity spectrum is self-similar, i.e., a power-law, as evidenced in numerous studies (see the review by Hennebelle & Falgarone 2012, and the references therein).

Turbulence in molecular clouds has been studied in a variety of scales and contexts. Larson (1981) found for the first time a power law relation between the velocity dispersion  $\sigma$  and the (projected, 2D) size  $L$  of molecular clouds  $\sigma_v \propto L^{0.38}$ . This power law form relation between the velocity dispersion and the size of molecular clouds is then called Larson's relation. Later observations established the now widely accepted index of 0.5 (Solomon et al. 1987; Falgarone et al. 1992; Heyer & Brunt 2004). The former index is close to the power law index 1/3 of incompressible turbulence, while the latter may indicate density fluctuations within molecu-

lar clouds (Vazquez-Semadeni & Gazol 1995), which is confirmed in observational studies (Brunt & Heyer 2002; Brunt 2003) and numerical simulations with increasing sophisticated physics and resolution (Ostriker et al. 2001; Offner et al. 2008; Kritsuk et al. 2013). However, recent studies on this topic bring more complications. Zhang et al. (2014) find in North American and Pelican molecular clouds a power law index of 0.43 for the Larson's relation, which deviates from the traditional value of 0.5. In another study, Heyer et al. (2009) showed that the normalization of the velocity dispersion-size relation molecular clouds,  $v_0 = \sigma_v/L^{1/2}$ , scales with the surface density of the clouds  $\Sigma$  as  $v_0 \sim \Sigma^{1/2}$ , indicating that molecular clouds are in self-gravitational equilibrium.

Traditionally, structure function methods (e.g. Brunt & Heyer 2002) and principal component analysis (PCA, Heyer & Schloerb 1997; Brunt 2003) are used for characterizing the turbulent velocity field. Recently, Qian et al. (2012) developed the core velocity dispersion (CVD) technique to study turbulence in the Taurus molecular cloud. This method uses the centroid velocity (average velocity of a core weighted with mass) of identified molecular cores to sample the velocity field of spatially and spectrally coherent structures in relatively dense gas. In this paper, we compare the characteristics of the CVD with the gas turbulence and examine whether CVD could trace the general motion of the underlying gas. Qian et al. (2012) found that the dispersion of the core velocities increases with distance, i.e.  $\text{CVD} \propto L_{2D}^{0.5}$  between 1 pc and 10 pc, which resembles Larson's relation (hereafter, we will attach the subscript 2D to  $L$  as  $L_{2D}$  and 3D to  $l$  as  $l_{3D}$  to emphasize the dimension of the spatial scales). Larson's relation can be explained by the velocity spectrum of a 3D turbulent velocity field (Kritsuk

\*LQ analysed the observational data and wrote the paper except the hydrodynamical simulation part.

†DL proposed the ideas to study the influence of thickness on the CVD. He also contributed to the paper text.

‡SO provided the hydrodynamical simulation, performed synthetic CO observations, wrote the hydrodynamical simulation part of the paper. She also made overall modification to the paper.

§ZP helped to analyse the observational data.

<sup>1</sup> National Astronomical Observatories, Chinese Academy of Sciences, Beijing, 100012, China

<sup>2</sup> Key Laboratory of Radio Astronomy, Chinese Academy of Sciences, Beijing, China

<sup>3</sup> Department of Astronomy, University of Massachusetts, Amherst, MA, USA

<sup>4</sup> Space Science Institute, Boulder, Colorado, USA

et al. 2013). There is a fundamental difference between the CVD- $L_{2D}$  relation and the turbulent velocity spectrum, in that the turbulent velocity spectrum is three-dimensional, while the spatial scale in the CVD- $L_{2D}$  relation is a projected (2D) scale.

In this work, we expanded upon the previous results and study the influence of the line-of-sight scale (thickness) on the CVD- $L_{2D}$  relation. We described our observational data in §2, presented our methods in §3, and discussed results in §4. In §5, we summarized our conclusions and addressed the potential application of the CVD in future studies.

## 2. OBSERVATIONAL DATA

The  $^{13}\text{CO}$  ( $J=1-0$ , 110.2014 GHz) data of Taurus in this work were obtained with the 13.7 m FCRAO telescope between 2003 and 2005. The map is centered at RA(2000.0) =  $04^{\text{h}}32^{\text{m}}44.6^{\text{s}}$ , Dec(2000.0) =  $24^{\circ}25'13.08''$ , with an area of  $\sim 98 \text{ deg}^2$ , and a noise level of 0.1 K (Narayanan et al. 2008). The velocity resolution is 0.266 km/s. The  $^{13}\text{CO}$  data of Perseus and Ophiuchus came from the COMPLETE database (Ridge et al. 2006)<sup>5</sup>, which were also observed with the FCRAO telescope. The velocity resolution is 0.066 km/s. The noise levels of Perseus and Ophiuchus are 0.15 K and 0.2 K, respectively.

Following Qian et al. (2012), we used the GAUSS-CLUMPS method in the Starlink software<sup>6</sup> to identify cores from the data cube. The lower thresholds of the peak intensity of cores were set to be 7 times the noise level (see Qian et al. 2012), which were about 0.7 K, 1.0 K, and 1.5 K for Taurus, Perseus, and Ophiuchus, respectively. In Taurus, Perseus, and Ophiuchus, 588, 693, and 270 cores were identified, respectively. The typical size of the cores is around 0.1 pc.

## 3. METHODS

In order to investigate the influence of the cloud thickness on the CVD- $L_{2D}$  relation, we used two approaches. In the first approach we statistically generate a sample of cores in a velocity field with second order structure function of index 0.5, which corresponds to an energy spectrum of index  $\beta = 2$ . In the second approach we perform hydrodynamic simulations of molecular clouds.

### 3.1. Calculation of the CVD

CVD stands for Core Velocity Dispersion, which is obtained as follows (Qian et al. 2012). First the difference of centroid velocity ( $\delta v$ ) and projected spatial distance ( $L_{2D}$ ) of each pair of cores are calculated. The distribution of  $\delta v$  in the  $\delta v - L_{2D}$  plane is in grey scale in the top panel of Figure 1 for the Taurus molecular cloud. Then we calculate the CVD, which is the mean square root of the values of  $\delta v$ , i.e.  $\text{CVD} \equiv \langle \delta v^2 \rangle^{1/2}$ , at different  $L_{2D}$  (see the green diamonds in the top panel of Figure 1). Figure 1 is similar to Figure 18 in Qian et al. (2012), but now we focus on the power-law-form CVD- $L_{2D}$  relation between 1 pc and 10 pc, which reflects the pattern of turbulent motion in Taurus.

In order to compare the CVD to a turbulence velocity spectrum, we fit a power law or a broken power law to

the CVD- $L_{2D}$  relation in this work. The break point of the broken power law is determined from the  $\log(\text{CVD}) - \log(L_{2D})$  plot by eye. The fitting error is estimated with a bootstrap method (Press et al. 1992). We construct 100 samples of core pairs based on the real sample of core pairs, in which every pair in each sample is randomly selected from the data. Then we fit parameters to these 100 samples, and the error is estimated by calculating the root of mean square of the fitted parameters. Since there is degeneracy between the normalization and the index of a power law function, for power law fitting through out this paper, the power law index is first obtained by fitting a linear function to the log-log data and then fixed in the subsequent fitting in linear space, meant to obtain the offset constant.

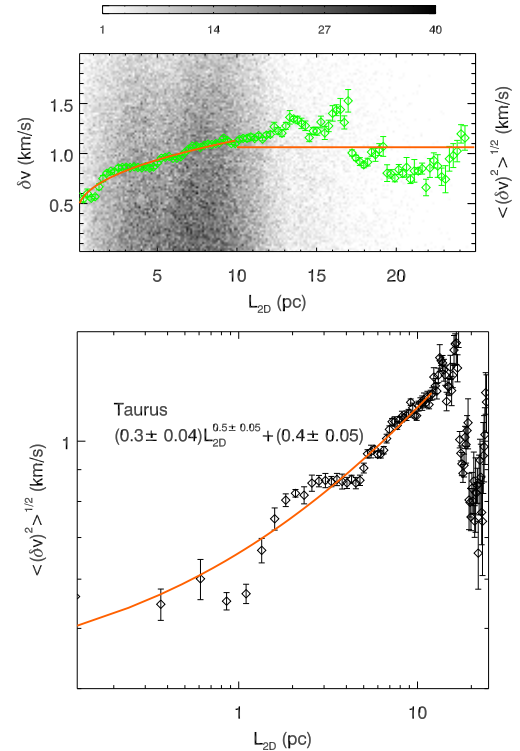


**Figure 1.** *Top:* Core velocity difference between each core pair,  $\delta v$ , and the core velocity dispersion ( $\text{CVD} \equiv \langle \delta v^2 \rangle^{1/2}$ ) vs. the projected separation,  $L_{2D}$ , of the cores for the Taurus molecular cloud. The background is an image of the number of data points in the  $\delta v - L_{2D}$  plane, with the grey scale (density bar at the top of the figure) showing the density of points. The green diamonds represent the CVD in each separation bin. The CVD data points with apparent separation  $0 \leq L_{2D} \leq 10$  pc can be fitted with a power law of CVD (km/s) =  $(0.3 \pm 0.04)L_{2D}^{0.5 \pm 0.05} + (0.4 \pm 0.05)$ . The horizontal line shows the mean CVD value, 1.1 km/s, of data points with  $L_{2D} > 10$  pc. *Bottom:* The CVD as a function of projected distance. The range of the power law fit is determined in this log-log scale plot. The fitting error is estimated with a bootstrap method.

### 3.2. Statistical Core Distribution Model

In order to study how well the core velocities correlate with the underlying velocity field and the cloud geometry, we formulate a simple statistical model, the fractional Brownian motion model, of cores within a turbulent molecular cloud. The core sample is generated

<sup>5</sup> <http://www.cfa.harvard.edu/COMPLETE/>

<sup>6</sup> <http://starlink.jach.hawaii.edu/starlink/>

with procedures similar to those used in generating a turbulent velocity field (Brunt & Heyer 2002; Miville-Deschênes et al. 2003). Theoretically, the root of mean square turbulent velocity at scale  $l$  (scale length in 3D),  $v_l$ , can be determined by the velocity fluctuations over scales smaller than  $l$ :

$$v_l^2 \sim \int_{2\pi/l}^{\infty} E(k) dk \propto \int_{2\pi/l}^{\infty} k^{-\beta} dk \propto l^{\beta-1}, \quad (1)$$

where  $k$  is the wave number. If we assume  $\langle v_l^2 \rangle^{1/2} \propto l^\gamma$ , the relation between  $\beta$  and  $\gamma$  will be  $\gamma = (\beta - 1)/2$  in 3D. By definition,

$$v_l^2 \sim \int v(k)^2 k^2 dk, \quad (2)$$

where  $v(k) \propto k^{-\delta}$ .

We first generate a 3D velocity field and put roughly 4000 cores on a randomly selected set of grid points. A simple way to do this follows the procedure below. First, we generate a Gaussian random field with dimension  $128 \times 128 \times 128$  on a 3D grid. Next, we perform a Fourier transform. Then, we process this field in the frequency domain to satisfy the desired power law distribution ( $\propto k^{-\delta}$ ). Finally, we perform an inverse Fourier transformation and normalize the generated field to fulfill the desired variance, which is related to the velocity dispersion.

### 3.3. Hydrodynamic Simulations and Synthetic Observations

We use hydrodynamic simulations to explore the effects of density/velocity correlations. We use the ORION adaptive mesh refinement (AMR) code to perform simulations of turbulent star-forming molecular clouds (Truelove et al. 1998; Klein 1999). The simulations use periodic boundary conditions and are meant to represent a piece of a typical low-mass star forming cloud similar to Taurus. The numerical methods we use are similar to previous calculations (e.g. Offner et al. 2009b, 2013), so we briefly describe the simulations here and refer the reader to these papers for additional details.

We compare the observations with snapshots from two simulations, each with different turbulent properties (see Table 1). Both simulations have a domain size of 10 pc, contain  $\sim 15,000 M_\odot$ , and have an initial gas temperature of 10 K. Simulation RT has a turbulent velocity dispersion of  $1.52 \text{ km s}^{-1}$ , such that it satisfies the observed linewidth-size relation at 10 pc,  $\sigma_{2D} = 0.72 R^{0.5} \text{ km s}^{-1}$  (e.g., McKee & Ostriker 2007). RT1 and RT2 correspond to two different output times for the RT simulation. They have ages of 0.65 Myr and 1.03 Myr, respectively. The turbulence is initialized by adding random velocity perturbations with an input power spectrum  $P(k) \propto k^0$  for input wave numbers in the range  $k = 1 \sim 2$ . Simulation HD has a velocity dispersion of  $1.06 \text{ km s}^{-1}$  and the turbulent perturbations have  $P(k) \propto k^{-2}$  for  $k = 1 \sim 10$ . The latter turbulent perturbations are generated in the same way as those used in section 3.2. To achieve a turbulent steady-state, in which the power-spectrum and density distribution function are constant in time, we inject the perturbations for two domain crossing times without self-gravity.

After turning on gravity, we continue injecting energy so that the velocity dispersion remains constant. Without continuous energy injection, the turbulence would decay as a result of dissipation in shocks over a crossing time (e.g. Stone et al. 1998; MacLow 1999). Once collapse begins, refinement is added to ensure that the Jeans criterion is satisfied for a Jeans number of  $N_J = 0.125$  (Truelove et al. 1997). We insert sink particles when the density exceeds the Jeans resolution on the maximum AMR level (Krumholz et al. 2004). HD adopts an isothermal equation of state, while RT solves the radiative transfer equation in the flux limited diffusion approximation; it also includes radiative feedback from the forming stars (Krumholz et al. 2007; Offner et al. 2009b). This heating, which is generally limited to regions near sink particles, has minimal impact on the turbulent properties.

RT and HD have  $512^3$  and  $256^3$  base grids with 2 and 4 AMR levels of refinement, respectively. Here, we only use the data on the base grid, which is comparable to the observational pixel resolution, to produce the synthetic observations (see below). Figure 2 shows the velocity energy spectra for the three snapshots. For low wave numbers ( $k = 1 \sim 4$ ) the energy spectrum is flatter than  $k^{-2}$ . It steepens above  $k \sim 20$  where dissipation occurs. The dissipation scale is set by the numerical grid size and typically occurs on a scale of a few grid cells.

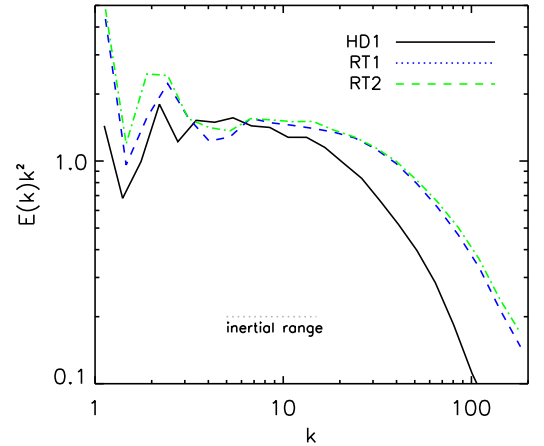


**Figure 2.** Simulated velocity energy spectra compensated by  $k^2$  for the hydrodynamic simulations. The grey dotted line indicates the inertial range.

In order to compare the simulations directly with the Taurus observations we post-process the outputs with the radiative transfer code RADMC-3D<sup>7</sup>. We use the Large Velocity Gradient (LVG) approach, which computes the molecule level populations by solving for radiative statistical equilibrium (Shetty et al. 2011). The input densities, temperatures, and velocities are supplied by the hydrodynamic simulations.

We model unresolved turbulent broadening by adopting a constant micro-turbulence parameter of  $0.1 \text{ km s}^{-1}$ . The  $\text{H}_2$  number density is defined as  $n_{\text{H}_2} = \rho / (2.8 m_p)$ ,

<sup>7</sup> <http://www.ita.uni-heidelberg.de/~dullemond/software/radmc-3d/>

where  $\rho$  is the gas density, the 2.8 factor accounts for the molecular weight of Helium. We assume a constant  $^{13}\text{CO}$  abundance of  $[^{13}\text{CO}/\text{H}_2]=2.5 \times 10^{-6}$  (Frerking et al. 1982; Langer & Penzias 1993), and we adopt the molecular collisional coefficients from Schöier et al. (2005). We compute the line emission for the velocities within  $\pm 5 \text{ km s}^{-1}$  of the line rest frequency and use a channel resolution of  $\Delta v = 0.039 \text{ km s}^{-1}$ .

To account for differences in resolution and sensitivity, we convolve the synthetic line data with a  $45''$  Gaussian beam, assuming that the simulated cloud lies at a distance of 140 pc. We re-bin the emission such that the pixel size is  $20''$  and the velocity channel width is  $0.26 \text{ km s}^{-1}$ . Finally, we add Gaussian random noise with a standard deviation of 0.3 K.

In order to assess the effects of cloud thickness on the observations, we perform the line transfer on input volumes of different extents along the line of sight. We compare the cases for line-of-sight thicknesses  $L$ ,  $\frac{1}{2}L$ ,  $\frac{1}{4}L$ ,  $\frac{1}{8}L$ , and  $\frac{1}{16}L$ , where  $L = 10 \text{ pc}$ . Table 2 summarizes all the RADMC-3D runs.

#### 4. RESULTS

##### 4.1. The CVD of Taurus, Perseus, and Ophiuchus

The observed Taurus CVD for cores identified in  $^{13}\text{CO}(1-0)$  is shown in Figure 1. In the scale range  $L_{2D} < 10 \text{ pc}$ , the CVD- $L_{2D}$  relation is well-fit by a power law given by  $\text{CVD} = (0.3 \pm 0.04)L_{2D}(\text{pc})^{0.5 \pm 0.05} + (0.4 \pm 0.05) \text{ km s}^{-1}$ . The characteristic scale of 10 pc can be clearly seen from the log scale plot in the bottom panel of Figure 1.

The solid line in Figure 3 shows the histogram of the core centroid velocities. The distribution is double-peaked, which could indicate two core populations. This might occur if the Taurus has distinct sub-regions with different line-of-sight velocities. One group has centroid velocities larger than 6 km/s and the other has centroid velocities smaller than 6 km/s. The former group of cores does not have a clear velocity gradient, but the latter group does ( $\nabla v \simeq 1 \text{ km/s/deg}$ ). A plot of the core centroid velocity versus right ascension as shown in Figure 4 also indicates that there are two core populations.

We performed the CVD analysis of each group of cores and found that the CVD- $L_{2D}$  relation for cores with centroid velocities larger than 6 km/s can be fitted by a broken power law with power law indices  $0.1 \pm 0.03$  ( $L_{2D} < 5 \text{ pc}$ ) and  $0.3 \pm 0.02$  ( $5 \text{ pc} < L_{2D} < 10 \text{ pc}$ ). Cores with centroid velocities smaller than 6 km/s can be fitted with an index of  $0.5 \pm 0.3$  (Figure 5). We fit and then subtract the velocity gradient  $1 \text{ km/s/deg}$  in the latter case and find that the resultant power law index is also 0.5.

We have performed a similar analysis for the Perseus and Ophiuchus molecular clouds. In Perseus, the cores do not divide into groups (dash-dotted line in Figure 3), although there is a velocity gradient of  $4 \text{ km/s/deg}$  among the cores (see Figure 7). We perform the fit again after subtracting the gradient and verify that the gradient does not affect our results. The CVD between  $0 \text{ pc} \leq L_{2D} \leq 7 \text{ pc}$  is nearly constant, about  $1.5 \text{ km/s}$ , while the upturn between  $7 \text{ pc} \leq L_{2D} \leq 13 \text{ pc}$  can be fitted with  $\text{CVD}(\text{km/s}) = (0.3 \pm 0.001)L_{2D}(\text{pc})^{0.6 \pm 0.01}$  (Figure 7). The break point (7 pc) is determined from the lower panel by eye. In Ophiuchus, the core veloc-

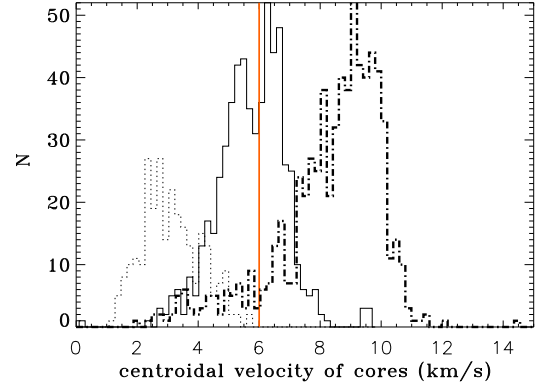


**Figure 3.** Solid line: Histogram of the central velocities of cores in the Taurus molecular cloud. There are clearly two groups of cores with different central velocities, divided by the solid line at 6 km/s. Dash-dotted line: Histogram of the central velocities of cores in Perseus. Dotted line: Histogram of the central velocities of cores in Ophiuchus.

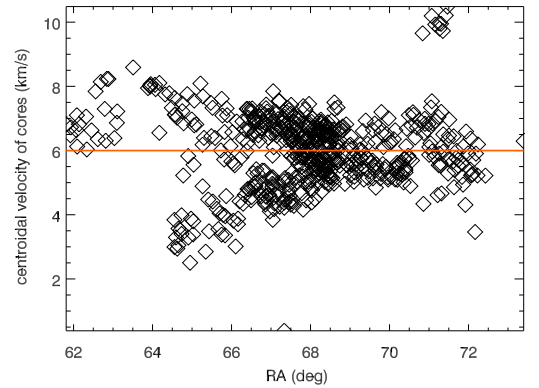


**Figure 4.** The centroid velocity of cores vs. RA. relation in the Taurus molecular cloud. There are two apparent core groups with the dividing line roughly lying at 6 km/s (solid line). One group of cores has a velocity gradient.

ity distribution is also centrally peaked (dotted line in Figure 3). There is no core velocity gradient (Figure 6), and we find that the CVD between  $0 \text{ pc} \leq L_{2D} \leq 3.5 \text{ pc}$  is nearly constant, about  $0.8 \text{ km/s}$ . The upturn in the range of  $3.5 \leq L_{2D} \leq 5 \text{ pc}$  can be fitted with  $\text{CVD}(\text{km/s}) = (0.5 \pm 0.05)L_{2D}(\text{pc})^{0.4 \pm 0.07} - (0.03 \pm 0.001)$  (Figure 8). The break point (3.5 pc) is determined from the lower panel by eye.

The breaks in Perseus (7 pc) and in Ophiuchus (3.5 pc) may indicate the thicknesses of the clouds (see discussion below equation 4 in section 4.3). We performed the statistical modeling mentioned in section 3.2. Figure 9 shows models with a range of relative thicknesses  $\mathcal{R}$ , with the fitted power law overlayed, which correspond to the gamma values in figure 10-12. The upturn feature is marginally seen.

##### 4.2. Influence of geometry

Previous studies of the Taurus molecular cloud found that the CVD follows a power law in the projected length scale (2D distance,  $L_{2D}$ ) with a power law index of 0.5

**Table 1**  
Simulation Properties

| Model <sup>a</sup> | $M(M_{\odot})$      | $\mathcal{M}$ | $L$ (pc) | $t_f$ (Myr) | $N^3$   | $\Delta x_{\min}$ (pc) |
|--------------------|---------------------|---------------|----------|-------------|---------|------------------------|
| RT1                | $1.475 \times 10^4$ | 14.0          | 10.0     | 0.65        | $512^3$ | 0.005                  |
| RT2                | $1.475 \times 10^4$ | 14.0          | 10.0     | 1.03        | $512^3$ | 0.005                  |
| HD1                | $1.475 \times 10^4$ | 10.0          | 10.0     | 1.06        | $256^3$ | 0.0025                 |

<sup>a</sup> Run name, total gas mass, domain length, analysis output time, base-grid size, and minimum cell size. RT1 and RT2 are two different output times for the same simulation. They have random perturbations in the range  $k = 1 \sim 2$  with  $P(k_{1-2}) \propto k^0$ . HD1 has random perturbations  $k = 1 \sim 10$  with  $P(k_{1-10}) \propto k^{-2}$ . All runs are first evolved for two crossing times without self-gravity and have an initial temperature of 10 K. RT1 and RT2 also include radiative feedback from forming stars (Offner et al. 2009).

**Table 2**  
RADMC Runs

| Model <sup>a</sup> | $N_x \times N_y \times N_z$ | View | $(L_x(\text{pc}), L_y(\text{pc}), L_z(\text{pc}))$ |
|--------------------|-----------------------------|------|--|
| RT1.L10z.M14       | $512 \times 512 \times 512$ | $z$  | (10, 10, 10)                                       |
| RT1.L5z.M14        | $512 \times 512 \times 256$ | $z$  | (10, 10, 5)  |
| RT1.L2.5z.M14      | $512 \times 512 \times 128$ | $z$  | (10, 10, 2.5)                                      |
| RT1.L0.125z.M14    | $512 \times 512 \times 64$  | $z$  | (10, 10, 0.125)                                    |
| RT1.L0.0625z.M14   | $512 \times 512 \times 32$  | $z$  | (10, 10, 0.0625)                                   |
| RT1.L10y.M14       | $512 \times 512 \times 512$ | $y$  | (10, 10, 10)                                       |
| RT1.L5y.M14        | $512 \times 512 \times 256$ | $y$  | (10, 10, 5)  |
| RT1.L2.5y.M14      | $512 \times 512 \times 128$ | $y$  | (10, 10, 2.5)                                      |
| RT2.L10y.M14       | $512 \times 512 \times 512$ | $y$  | (10, 10, 10)                                       |
| HD1.L10z.M10       | $256 \times 256 \times 256$ | $z$  | (10, 10, 10)                                       |
| HD1.L5z.M10        | $256 \times 256 \times 128$ | $z$  | (10, 10, 5)  |

<sup>a</sup> Model name, input RADMC grid size, line-of-sight view, and domain size. We adopt a constant micro-turbulence value of 0.1 km/s and a doppler catching parameter of 0.25 for all runs.

(Qian et al. 2012). It resembles the Larson’s relation. The main difference between these two relations is that the Larson’s relation is based on the integrated properties of different clouds, while the centroid velocity of the cores used in the CVD calculation probes the systemic velocities of spatially and spectrally ‘coherent’ clumps of gas.

In principle, if a cloud has an infinite thickness (but finite optical depth), the CVD- $L_{2D}$  will not hold. The only reason that there is a power law relation between the CVD and the projected length scale  $L_{2D}$  is that the cores are distributed in a limited range along the line of sight direction (‘thickness’), in which case 2D still bears resemblance to 3D. The difference between 2D and 3D description of turbulence have been studied in some works based on the line centroid velocity analysis (e.g. Miville-Deschênes et al. 2003; Brunt & Mac Low 2004). In the case **where** the line of sight scale is much smaller than the transverse scale, **the exponent of the  $\sigma_v - L_{2D}$  relation (section 4.1),  $\gamma_{2D}$ , is related to the exponent of the second order structure function  $\gamma_{3D}$  by  $\gamma_{2D} = \gamma_{3D}$  (Miville-Deschênes et al. 2003).** Here,  $\gamma_{2D/3D}$  is the power law index of the  $\sigma_v - L_{2D/3D}$  relation (section 3.2). However, in general, the density inhomogeneity will produce  $\gamma_{2D} \approx \gamma_{3D} \approx 0.5$ . When the effect of the density inhomogeneity is diminished in the late time of decaying turbulence, the relation between the 2D power law index  $\gamma_{2D}$  and the 3D one  $\gamma_{3D}$  is  $\gamma_{2D} \approx \gamma_{3D} + 0.5$  (Brunt & Mac Low 2004). Thus it is theoretically expected that the depth of the cloud **would**

**affect** the relation between velocity fluctuations (e.g., in the CVD) and projected scale. We explore this effect here using the simulations described in **sections 3.2 and 3.3.**

As a limiting case of large thickness, in the statistical (fractional Brownian motion) modelling mentioned in section 3.2, we used a  $128 \times 128 \times 128$  grid (with Relative Thickness  $\mathcal{R} \equiv z/x = 1$ ) to generate the velocity field. We distribute 4000 cores randomly on the grid points (top panel of Figure 10). Each core is assigned a centroid velocity corresponding to the velocity at its grid location. Thus, we assume each core perfectly traces the underlying velocity field. The power law index of the core velocities is then fitted as shown in Figure 10. The distribution of cores in the  $128 \times 128 \times 128$  grid is shown in the top panel of Figure 10. Each dot represents a core. The bottom panel of Figure 10 **shows the plots of** the power law index of the CVD- $L_{2D}(l_{3D})$  relation ( $\gamma$ ) versus the power law index of the energy spectrum ( $\beta$ ) of the velocity field. Circles are results from the CVD- $l_{3D}$  relation, while triangles are from the CVD- $L_{2D}$  relation. For  $1 < \beta < 3$  the relation between  $\gamma$  and  $\beta$  of the 3D scenario is close to the theoretical relation between  $\beta$  and  $\gamma$ ,  $\gamma = (\beta - 1)/2$ , however, the 2D scenario is quite different, with the CVD- $L_{2D}$  slope being consistent with zero. This reflects the difference between  $L_{2D}$  and  $l_{3D}$  when the thickness is large. For  $\beta > 3$ ,  $\gamma$  asymptotically approaches unity (Brunt & Heyer 2002).

As a limiting case of small thickness, we consider a  $128 \times 128 \times 4$  slab (the relative thickness  $\mathcal{R} = 1/32$ )



**Table 3**  
Summary of data fitting

| Model <sup>a</sup>                | Power law index              |
|-----------------------------------|------------------------------|
| Taurus cores                      | $0.5 \pm 0.05$               |
| Taurus cores ( $> 6$ km/s)        | $0.3 \pm 0.02$               |
| Taurus cores ( $\leq 6$ km/s)     | $0.5 \pm 0.3$                |
| Taurus $^{12}\text{CO}$ gas       | $0.4 \pm 0.01$               |
| Taurus $^{13}\text{CO}$ gas       | $0.5 \pm 0.03, 0.2 \pm 0.01$ |
| Perseus cores (0 pc $\sim$ 7 pc)  | $0.01 \pm 0.004$             |
| Perseus cores (7 pc $\sim$ 13 pc) | $0.6 \pm 0.01$               |
| Ophiuchus cores                   | $0.01 \pm 0.01$              |
| RT1.L0.0625z.M14                  | $0.2 \pm 0.1$                |
| RT1.L2.5z.M14                     | $0.05 \pm 0.11$              |
| RT1.L5z.M14                       | $0.05 \pm 0.01$              |
| RT1.L10z.M14                      | $0.1 \pm 0.005$              |
| HD1.L10z.M10                      | $0.05 \pm 0.02$              |

<sup>a</sup> Models from Table 2 are only listed if a sufficient number of cores is identified by GAUSSCLUMPS to perform the analysis.

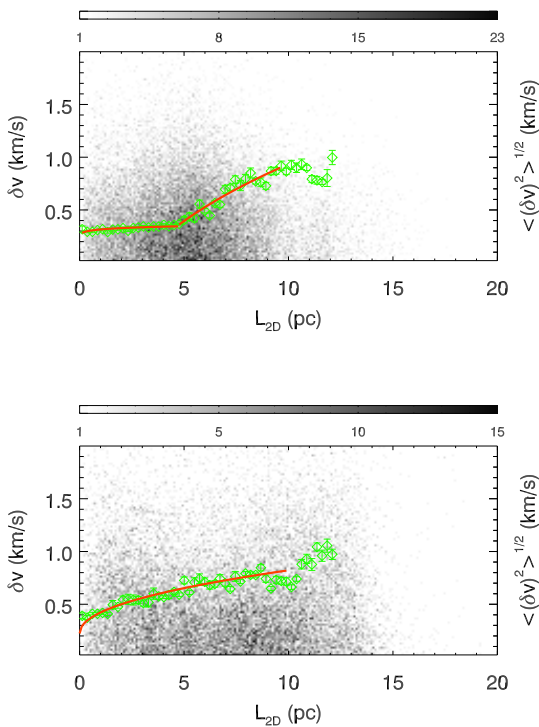


**Figure 5.** The CVD plot of the two group of cores in Figure 4: *top*: For the case with core centroid velocity greater than 6 km/s, two power laws are needed to fit the data, the power law indices are  $0.1 \pm 0.03$  ( $L_{2D} < 5$  pc) and  $0.3 \pm 0.02$  ( $5 \text{ pc} < L_{2D} < 10$  pc), respectively; *bottom*: the case with core centroid velocity lower than 6 km/s, the fitted power law index of the CVD- $L_{2D}$  relation is  $0.5 \pm 0.3$ .

from the previous  $128 \times 128 \times 128$  grid ( $\mathcal{R} = 1$ ) and put 4000 cores randomly on the grid points (Figure 11). The power law index of the CVD- $L_{2D}$  ( $l_{3D}$ ) relation is then fitted based on this core sample (Figure 11). The distribution of cores in a  $128 \times 128 \times 4$  grid is shown in Figure 11. The bottom panel of Figure 11 shows the power law index of the **CVD- $L_{2D}$ ( $l_{3D}$ ) relation** ( $\gamma$ ) as a function of the power law index of the energy spectrum ( $\beta$ ) of the velocity field. As in Figure 10, the circles indicate results from the three-dimensional CVD ( $l_{3D}$ ) relation,

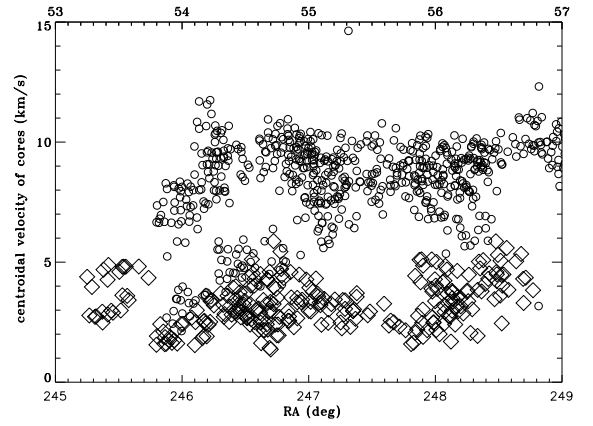


**Figure 6.** The centroid velocity of cores vs. RA. in Perseus (diamond, with the top x axis) and Ophiuchus (circle, with the bottom x axis).

while triangles are from the projected CVD relation. For  $1 < \beta < 3$  the relation between  $\gamma$  and  $\beta$  of both 3D and 2D relation is close to the theoretical relation between  $\beta$  and  $\gamma$ ,  $\gamma = (\beta - 1)/2$ . For  $\beta > 3$ ,  $\gamma$  asymptotically approaches unity (Brunt & Heyer 2002). The 3D and 2D scenarios are now similar. This is natural since the 2D length scale of a thin slab is approximately equal to the 3D length scale.

The panels in Figure 12 show the dependence of the  $\beta$ - $\gamma$  relation on the thickness of a cloud, where  $\mathcal{R}$  is  $1/32, 1/16, 1/12, 1/8, 1/5, 1/4, 1/2$  and  $1$ . We find that there is a critical relative thickness of  $\mathcal{R} \approx 1/10 - 1/8$ , above which the CVD- $L_{2D}$  relation significantly deviates from the CVD- $l_{3D}$  relation. This deviation is larger for steeper energy spectra. **Since the CVD- $L_{2D}$  relation for Perseus and Ophiuchus is flat below 7 pc and 3.5 pc, their thickness/transverse extent ratio must be  $\mathcal{R} > 1/10 - 1/8$ . With transverse extents of 16 pc and 8 pc for Perseus and Ophiuchus respectively, this corresponds to a thickness  $h > 1.6 \text{ pc} - 2.0 \text{ pc}$  for Perseus and  $h > 0.8 \text{ pc} - 1.0 \text{ pc}$  for Ophiuchus. Conversely, the CVD- $L_{2D}$  relation for Taurus is consistent with a  $\mathcal{R} < 1/10 - 1/8$  or  $h < 2.5 \text{ pc} - 3 \text{ pc}$ .**

To further constrain the depth of molecular clouds, we have developed a simple geometrical model of how the

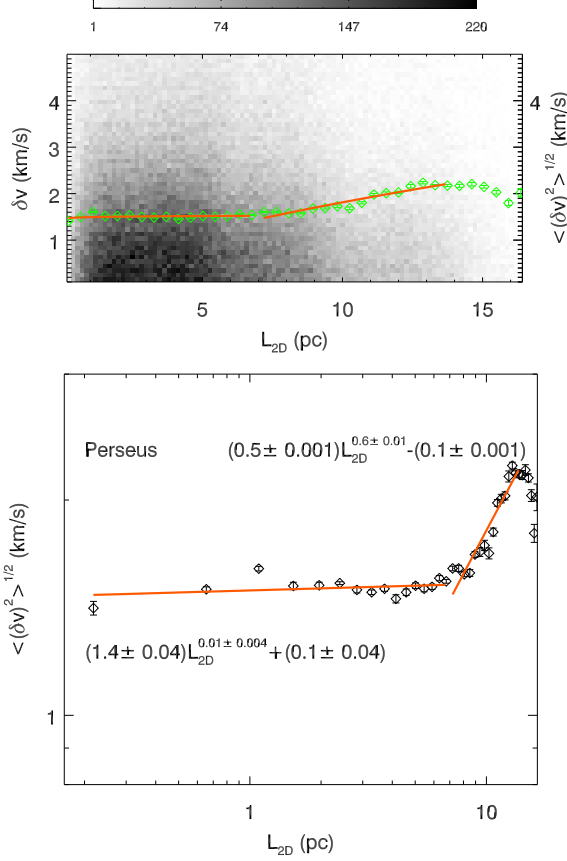


**Figure 7.** Similar plot to Figure 1, for Perseus molecular cloud. The CVD data points with apparent separation  $0 \leq L_{2D} \leq 7$  pc can be fitted with a power law of  $\text{CVD}(\text{km/s}) = (1.4 \pm 0.04)L_{2D}(\text{pc})^{0.01 \pm 0.004} + (0.1 \pm 0.04)$ . While those points in  $7 \leq L_{2D} \leq 13$  pc can be fitted with  $\text{CVD}(\text{km/s}) = (0.5 \pm 0.001)L_{2D}(\text{pc})^{0.6 \pm 0.01} - (0.1 \pm 0.001)$ . The break point (7 pc) is determined from the lower panel by eye.

integrated linewidth of a cloud depends on its transverse scale and thickness. This is discussed in the next section (section 4.3).

#### 4.3. Constraining cloud thickness from the linewidth-size relation

In order to understand this critical value of the relative thickness  $\mathcal{R}$ , we perform a simple analysis of the relation between the linewidth  $\sigma$  and 2D/3D scale  $L_{2D}/l_{3D}$ , and compare with the observational data. For a cloud with an energy spectrum of index  $\beta = 2$  the integrated linewidth is related to the 3D size by

$$\sigma \propto l_{3D}^{0.5}, \quad (3)$$

where  $l_{3D} = \sqrt{L_{2D}^2 + h^2}$ ,  $h$  is a typical scale along the line of sight of the molecular cloud. So we have

$$\sigma \propto \left( \sqrt{L_{2D}^2 + h^2} \right)^{0.5}. \quad (4)$$

In the limit of  $L_{2D} \gg h$ , the above two relations have approximately the same function form. In the limit of  $L_{2D} \ll h$ ,  $\sigma$  would not depend on  $L_{2D}$ . The two functions are illustrated in Figure 13. The specific value of

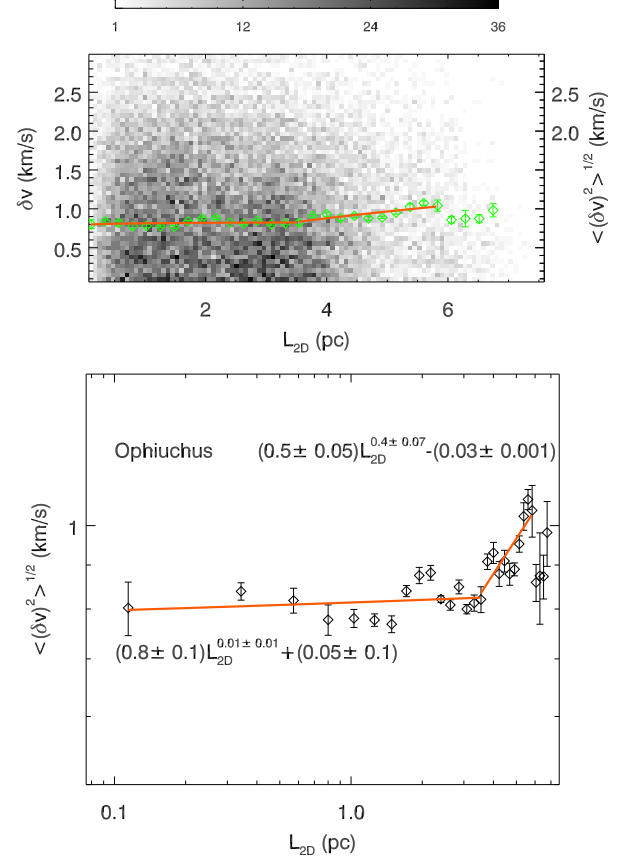


**Figure 8.** Similar plot to Figure 1, for Ophiuchus. The CVD data points with apparent separation  $0 \leq L_{2D} \leq 3.5$  pc can be fitted with a power law of  $\text{CVD}(\text{km/s}) = (0.8 \pm 0.1)L_{2D}(\text{pc})^{0.01 \pm 0.01} + (0.05 \pm 0.1)$ . Those points in  $3.5 \leq L_{2D} \leq 5$  pc can be fitted with  $\text{CVD}(\text{km/s}) = (0.5 \pm 0.05)L_{2D}(\text{pc})^{0.4 \pm 0.07} - (0.03 \pm 0.001)$ . The break point (3.5 pc) is determined from the lower panel by eye.

$\mathcal{R} = 1/10 - 1/8$  of the threshold is not clear from this figure, although the general trend that the difference between the  $\sigma$ - $L_{2D}$  relation and the  $\sigma$ - $l_{3D}$  relation becomes small at large transverse scales is clear.

We have applied this simple geometric model to Taurus, Perseus, and Ophiuchus. We selected random locations in Taurus and measured the average linewidth in groups of concentric circular regions centered on these locations. This analysis gives a lower limit to the overall thickness of Taurus. The lower envelope of the points on the  $\sigma - L_{2D}(l_{3D})$  plane provides a lower limit on the average thickness of the cloud. This lower envelope can be fitted with  $(\sigma/v_0) = \left( \sqrt{(L_{2D}/h)^2 + 1} \right)^{1/2}$  (Figure 13), and  $v_0 = 0.3$  km/s,  $h = 0.7$  pc.

We applied a similar analysis to the Perseus (Figure 14) and Ophiuchus (Figure 15) molecular clouds and found that the lower envelope of the points on the  $\sigma - L_{2D}(l_{3D})$  plane is nearly flat in both clouds. Note that Perseus and Ophiuchus are elongated, so the spatial dynamic range for concentric circular regions average is smaller than that of CVD analysis. The fitted parameters are  $v_0 = 0.6$  km/s,  $h = 3.6$  pc for Perseus, and  $v_0 = 0.4$  km/s,  $h = 2.0$  pc for Ophiuchus. Note the thicknesses  $h$  of Perseus and Ophiuchus are both lower limits, since the upturn as Taurus

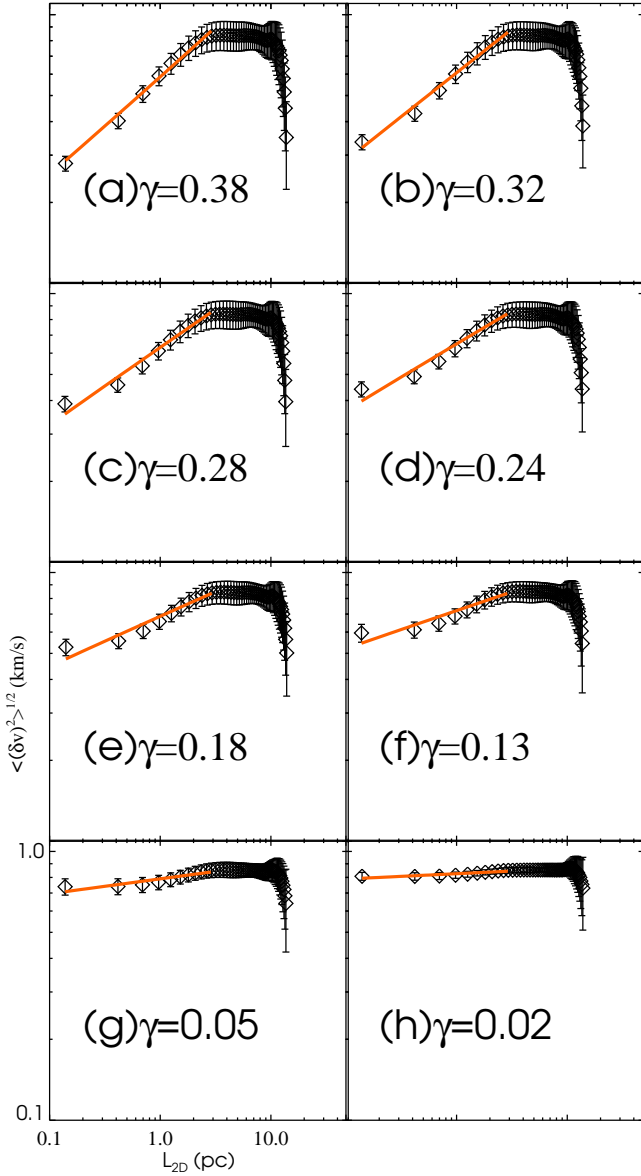


Figure 9. CVD- $L_{2D}$  plots similar to Figure 1, for fractional Brownian motion model ( $\beta = 2$ , see equation 1) of cores distributed in grids with relative thicknesses: (a) 1/32; (b) 1/16; (c) 1/10; (d) 1/8; (e) 1/5; (f) 1/4; (g) 1/2; (h) 1. The power law is fitted to the data points with  $0.1 \text{ pc} < L_{2D} < 3 \text{ pc}$ .

is not seen.

In this work, the thickness of a molecular cloud has been estimated with the slope of the CVD- $L_{2D}$  relation, the fitting to the lower envelope of the  $\sigma$ - $L_{2D}$  relation for all the three clouds, and the upturn location of the CVD- $L_{2D}$  relation for Perseus and Ophiuchus. 1) Based on the slope of the CVD- $L_{2D}$  relation, we conclude that the relative thickness  $\mathcal{R}$  of Taurus is smaller than 1/10-1/8, while  $\mathcal{R}$  of Perseus and Ophiuchus are larger than 1/10-1/8. The relevant transverse scales are about 25 pc, 16 pc, and 8 pc for Taurus, Perseus, and Ophiuchus, respectively. The estimated up-

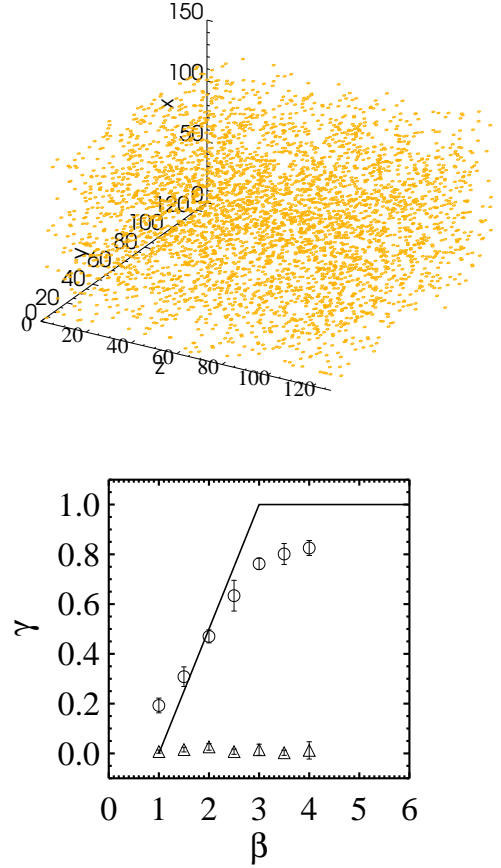
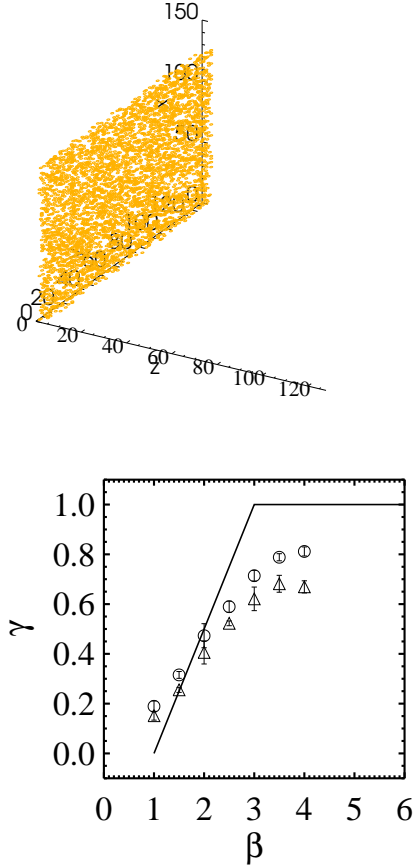


Figure 10. *Top*: Distribution of cores in a  $128 \times 128 \times 128$  grid. Each dot represents a core. *Bottom*: Relation between the power law index of energy spectrum ( $\beta$ , see equation 1) and the power law index of the CVD- $L_{2D}$  ( $l_{3D}$ ) relation ( $\gamma$ ). The  $1 < \beta < 3$  part of the solid line shows the theoretical relation between  $\beta$  and  $\gamma$ ,  $\gamma = (\beta - 1)/2$ . For  $\beta > 3$ ,  $\gamma$  asymptotically approaches unity. The circles (3D) and triangles (2D) are the results of the model.

per limit of the thickness of Taurus is 2.5 pc-3.0 pc. The estimated lower limits of the thickness of Perseus and Ophiuchus are 1.6 pc-2.0 pc and 0.8 pc-1.0 pc, respectively. 2) The characteristic thickness  $h$  of Taurus is 0.7 pc from the fitting to the lower envelope of the  $\sigma$ - $L_{2D}$  relation, which is consistent with the upper limit obtained in 1). The lower limits of the thickness  $h$  of Perseus and Ophiuchus are 3.6 pc and 2.0 pc, respectively. 3) The thicknesses possibly indicated by the upturn location of the CVD- $L_{2D}$  relation of Perseus and Ophiuchus are 7 pc and 3.5 pc, respectively. They are consistent with the lower limit obtained in 1) and 2).

The results are consistent with previous studies. For example, Arce et al. (2011) used the morphologies of bubbles within Perseus to conclude that its thickness is about 15% to 30% of its transverse scale. This is consistent with our conclusion that the depth of Perseus is larger than 15% of its projected size. In addition, (Loren 1989) find that the linewidth-size relation may not hold in Ophiuchus, which could partially explain the flat CVD slope we find. Enoch et al. (2008) find that the average dust extinction of Ophiuchus is much higher than that of other nearby clouds of similar projected size. This can





**Figure 11.** Similar to figure 10, for a  $128 \times 128 \times 4$  grid.

be explained if Ophiuchus is extended along the line-of-sight, and thus,  $\mathcal{R} \gg 1/10 - 1/8$ . The upturning point of the CVD in Figure 7 and Figure 8 may also be an indicator of the thickness of the clouds. In Figures 13, 14 and 15, the linewidth at the flattened part of the linewidth-size relation is 0.3 km/s to 0.6 km/s, which is larger than the thermal linewidth (at 10 K, the thermal linewidth of  $^{12}\text{CO}$  is about 0.07 km/s). The flattening of the linewidth-size relation is little affected by the thermal broadening.

#### 4.4. Influence of the turbulence

We used hydrodynamic simulations to study the impact of density-velocity correlations on projection effects (e.g. Brunt & Mac Low 2004). The transverse scale of the simulated clouds is 10 pc, and we varied the cloud thickness from 10 pc to 0.625 pc, by considering thinner sub-sections of the simulated clouds. When the thickness is smaller than 2.5 pc ( $\mathcal{R} < 1/4$ ), there are not enough cores in the 3D data cubes, so the errors are larger.

Figure 16 shows the CVD- $L_{2D}$  relation for cases of various cloud thicknesses. The CVD- $L_{2D}$  relations with relative thickness  $\mathcal{R} > 1/10 - 1/8$  are nearly flat, consistent with the influence of thickness on the CVD- $L_{2D}$  relation discussed in last section.

It is likely that the centroid velocity of cores is affected little by the global cloud Mach number (see also Offner et al. 2009a). In fact, there is a no simple correspondence between the density distribution and the distribution of cores (Padoan & Nordlund 2002). In some cases,

the temperature, mean density, type of driving, scale of driving are as important or even more important. If the CVD is primarily inherited from the cloud turbulent velocities, then we would not expect the CVD power index to depend on the global velocity dispersion, which simply sets the normalization of the cloud energy.

#### 5. CONCLUSION AND DISCUSSION

We studied the relationship between the core velocity dispersion (CVD) and the projected separation of cores ( $L_{2D}$ ) in molecular clouds. We compared the results with an analytic model and hydrodynamic simulations. We come to the following conclusions.

1) CVD is based on core centroid velocities, which reflects collective properties of dense gas condensations, thus is less affected by density fluctuations (c.f. Brunt & Mac Low 2004) and more sensitive to viewing geometry.

2) The relation between core velocities as a function of  $L_{2D}$  and  $l_{3D}$  is the same when the relative thickness  $\mathcal{R}$  of a cloud (the ratio of cloud length to cloud depth along the line of sight) is smaller than  $1/10$  to  $1/8$ . This result can potentially be used to constrain the line-of-sight cloud dimension, which is hard to measure directly. A simple functional fit to the CVD index and/or  $h$  in equation 4 can potentially be used to provide a limit to the thickness (line of sight dimension) of a cloud.

3) The CVD- $L_{2D}$ ( $l_{3D}$ ) in the Taurus molecular cloud can be fitted by a power law with an index of 0.5, resembling Larson's linewidth-size relation. This may indicate that the  $^{13}\text{CO}$  cores in Taurus are distributed in a volume that is thinner than **2.5 pc-3.0 pc, corresponding to  $1/10$  to  $1/8$  of the transverse cloud scale.** Performing the same analysis we conclude that the relative thickness  $\mathcal{R}$  of Perseus and Ophiuchus is larger than  $1/10$ - $1/8$ . **The corresponding lower limits of the thicknesses are 1.6 pc-2.0 pc for Perseus, and 0.8 pc-1.0 pc for Ophiuchus.**

4) We conclude that the thickness of a molecular cloud can be measured by using average line profiles in concentric regions of different sizes, where the  $\sigma$ - $L_{2D}$  relation flattens at small scales. **The characteristic thickness  $h$  of Taurus is 0.7 pc. The lower limits of the characteristic thicknesses  $h$  of Perseus and Ophiuchus are 3.6 pc and 2.0 pc, respectively.**

Our conclusions are consistent with priors observations, in which the scale and morphology of shells within the clouds indirectly constrains the cloud thickness (Arce et al. 2011; Li et al. 2015). This method provides a promising means of probing the cloud depth in regions where shells arising from stellar feedback are sparse or absent. In future works, we will apply this analysis to more diverse regions, e.g. molecular clouds with different column densities.

This work is partly supported by China Ministry of Science and Technology under State Key Development Program for Basic Research (2012CB821800, 2015CB857100) and the National Natural Science Foundation of China No. 11373038, No. 11373045, Strategic Priority Research Program of the Chinese Academy of Sciences, No. XDB09010302. SSR0 acknowledges support from NASA through Hubble Fellowship grant # 51311.01 awarded by the Space Telescope Science Institute, which is operated by the Association of Universities

for Research in Astronomy, INC., for NASA, under contract NAS 5-26555. The ORION calculations were performed on the Trestles XSEDE cluster and on the Yale University Omega cluster.

## REFERENCES

- Arce, H. G., Borkin, M. A., Goodman, A. A., et al. 2011, *ApJ*, 742, 105
- Blitz, L., Williams, J. P., 1997, *ApJ*, 488, L145
- Brunt, C. M. 2003, *ApJ*, 583, 280
- Brunt, C. M., & Heyer, M. H. 2002, *ApJ*, 566, 276
- Brunt, C. M., & Mac Low, M.-M. 2004, *ApJ*, 604, 196
- Enoch, M. L., Evans, II, N. J., Sargent, A. I., et al. 2008, *ApJ*, 684, 1240
- Falgarone, E., Puget, J.-L., & Perault, M. 1992, *A&A*, 257, 715
- Frerking, M. A., Langer, W. D., & Wilson, R. W. 1982, *ApJ*, 262, 590
- Hennebelle, P., & Falgarone, E. 2012, *A&A Rev.*, 20, 55
- Heyer, M., Krawczyk, C., Duval, J., & Jackson, J. M. 2009, *ApJ*, 699, 1092
- Heyer, M. H., & Brunt, C. M. 2004, *ApJ*, 615, L45
- Heyer, M. H., & Schloerb, F. 1997, *ApJ*, 475, 173
- Klein, R. I. 1999, *Journal of Computational and Applied Mathematics*, 109, 123
- Kritsuk, A. G., Lee, C. T., & Norman, M. L. 2013, *MNRAS*, 436, 3247
- Krumholz, M. R., Klein, R. I., & McKee, C. F. 2007, *ApJ*, 656, 959
- Krumholz, M. R., McKee, C. F., & Klein, R. I. 2004, *ApJ*, 611, 399
- Langer, W. D., & Penzias, A. A. 1993, *ApJ*, 408, 539
- Larson, R. B. 1981, *MNRAS*, 194, 809
- Li, H. X., Li, D., Qian, L., Xu, D., Goldsmith, P. F., Noriega-Crespo, A., Wu, Y. F., Song, Y. Z., Nan, R. D. 2015, *ApJS* accepted.
- Li, H.-B., & Houde, M. 2008, *ApJ*, 677, 1151
- Loren, R. B. 1989, *ApJ*, 338, 925
- MacLow, M.-M. 1999, *ApJ*, 524, 169
- McKee, C. F., & Ostriker, E. C. 2007, *ARA&A*, 45, 565
- Miville-Deschênes, M.-A., Levrier, F., & Falgarone, E. 2003, *ApJ*, 593, 831
- Narayanan, G., Heyer, M. H., Brunt, C., et al. 2008, *ApJS*, 177, 341
- Offner, S. S. R., Bisbas, T. G., Viti, S., & Bell, T. A. 2013, *ApJ*, 770, 49
- Offner, S. S. R., Hansen, C. E., & Krumholz, M. R. 2009a, *ApJ*, 704, L124
- Offner, S. S. R., Klein, R. I., McKee, C. F., & Krumholz, M. R. 2009b, *ApJ*, 703, 131
- Offner, S. S. R., Krumholz, M. R., Klein, R. I., & McKee, C. F. 2008, *AJ*, 136, 404
- Ostriker, E. C., Stone, J. M., & Gammie, C. F. 2001, *ApJ*, 546, 980
- Padoan, P., & Nordlund, Å., 2002, *ApJ*, 576, 870
- Press, W. H., Teukolsky, S. A., Vetterling, W. T., & Flannery, B. P. 1992, *Numerical recipes in FORTRAN. The art of scientific computing*
- Qian, L., Li, D., & Goldsmith, P. F. 2012, *ApJ*, 760, 147
- Ridge, N. A., Di Francesco, J. and Kirk, H., et al. 2006, *AJ*, 131, 2921
- Schöier, F. L., van der Tak, F. F. S., van Dishoeck, E. F., & Black, J. H. 2005, *A&A*, 432, 369
- Shetty, R., Glover, S. C., Dullemond, C. P., & Klessen, R. S. 2011, *MNRAS*, 412, 1686
- Solomon, P. M., Rivolo, A. R., Barrett, J., & Yahil, A. 1987, *ApJ*, 319, 730
- Stone, J. M., Ostriker, E. C., & Gammie, C. F. 1998, *ApJ*, 508, L99
- Truelove, J. K., Klein, R. I., McKee, C. F., et al. 1997, *ApJ*, 489, L179+
- Truelove, J. K., Klein, R. I., McKee, C. F., et al. 1998, *ApJ*, 495, 821
- Vazquez-Semadeni, E., & Gazol, A. 1995, *A&A*, 303, 204
- Zhang, S., Xu, Y., & Yang, J. 2014, *AJ*, 147, 46

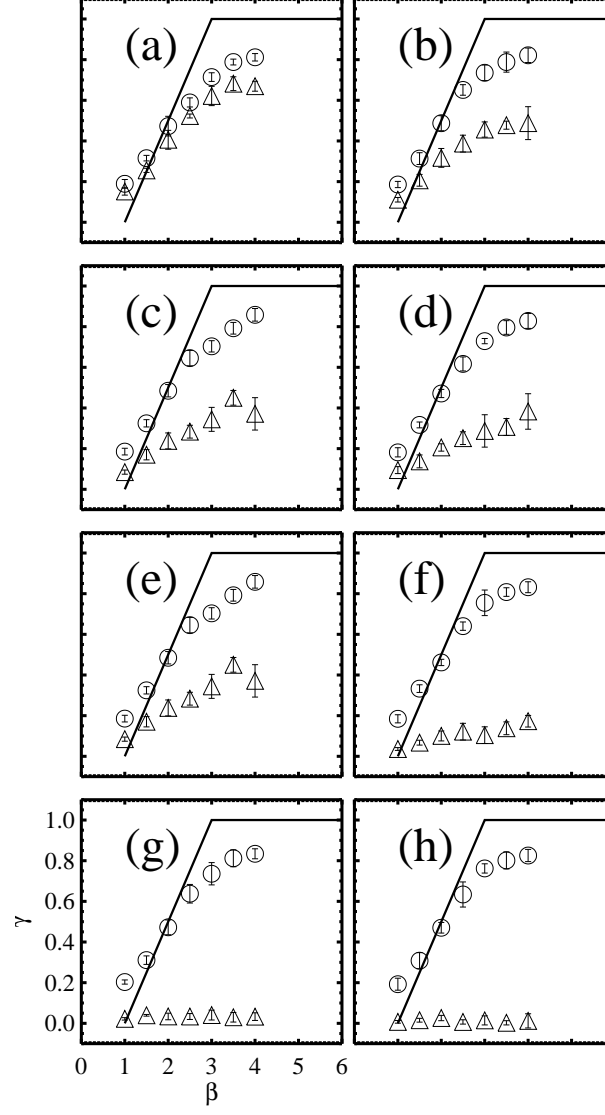


**Figure 12.** Relation between the power law index of energy spectrum ( $\beta$ ) and the power law index of the velocity field ( $\gamma$ ). The  $1 < \beta < 3$  part of the solid line shows the theoretical relation between  $\beta$  and  $\gamma$ ,  $\gamma = (\beta - 1)/2$ . The circles (3D) and triangles (2D) are the results of the model. Relative thicknesses in each panel: (a) 1/32; (b) 1/16; (c) 1/10; (d) 1/8; (e) 1/5; (f) 1/4; (g) 1/2; (h) 1.

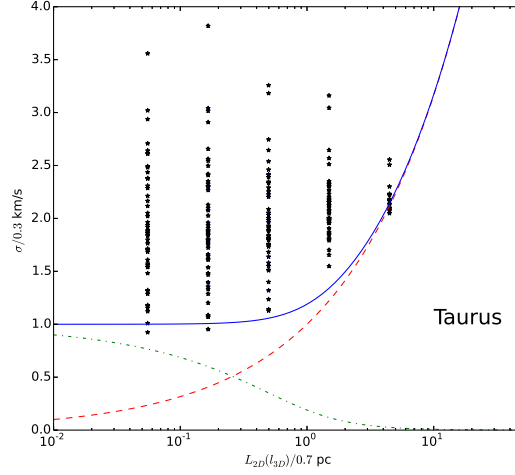


**Figure 13.** The solid line denotes the function  $(\sigma/v_0) = \left(\sqrt{(L_{2D}/h)^2 + 1}\right)^{1/2}$ , while the dashed line represents the function  $(\sigma/v_0) = (l_{3D}/h)^{1/2}$ . It can be seen that the difference becomes small at large  $L_{2D}/h$ .  $\sigma$  is normalized with a characteristic velocity  $v_0 = 0.3$  km/s, while  $L_{2D}(l_{3D})$  is normalized with thickness  $h = 0.7$  pc. The difference between these two functions is plotted with dash-dotted line. The asterisks show the linewidth measured at different scales. The lower envelope of these points probes the thinnest part of the cloud (cf. Li & Houde 2008). It flattens at the small scales.

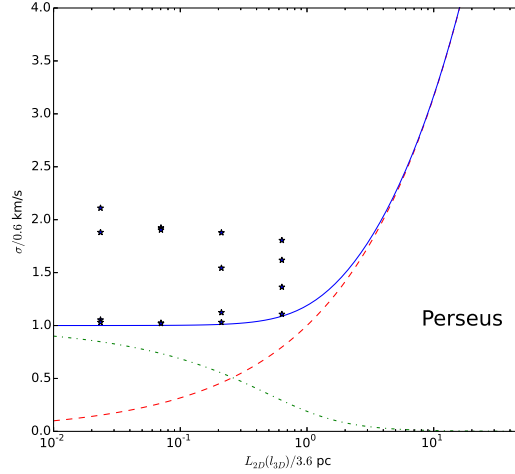


**Figure 14.** The same analysis of Perseus molecular cloud as Figure 13. The characteristic velocity  $v_0$  and the thickness  $h$  are 0.6 km/s and 3.6 pc, respectively. Since the upturn similar to that in figure 13 is not clearly seen, here  $h$  is only a lower limit of the thickness of Perseus.

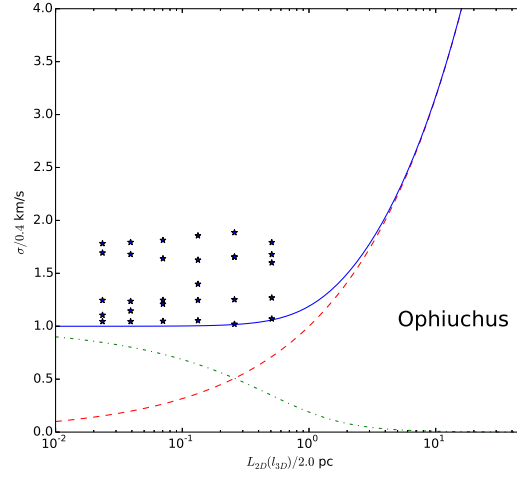


**Figure 15.** The same analysis of Ophiuchus molecular cloud as Figure 13. The characteristic velocity  $v_0$  and the thickness  $h$  are 0.4 km/s and 2.0 pc, respectively. Since the upturn similar to that in figure 13 is not clearly seen, here  $h$  is only a lower limit of the thickness of Ophiuchus.



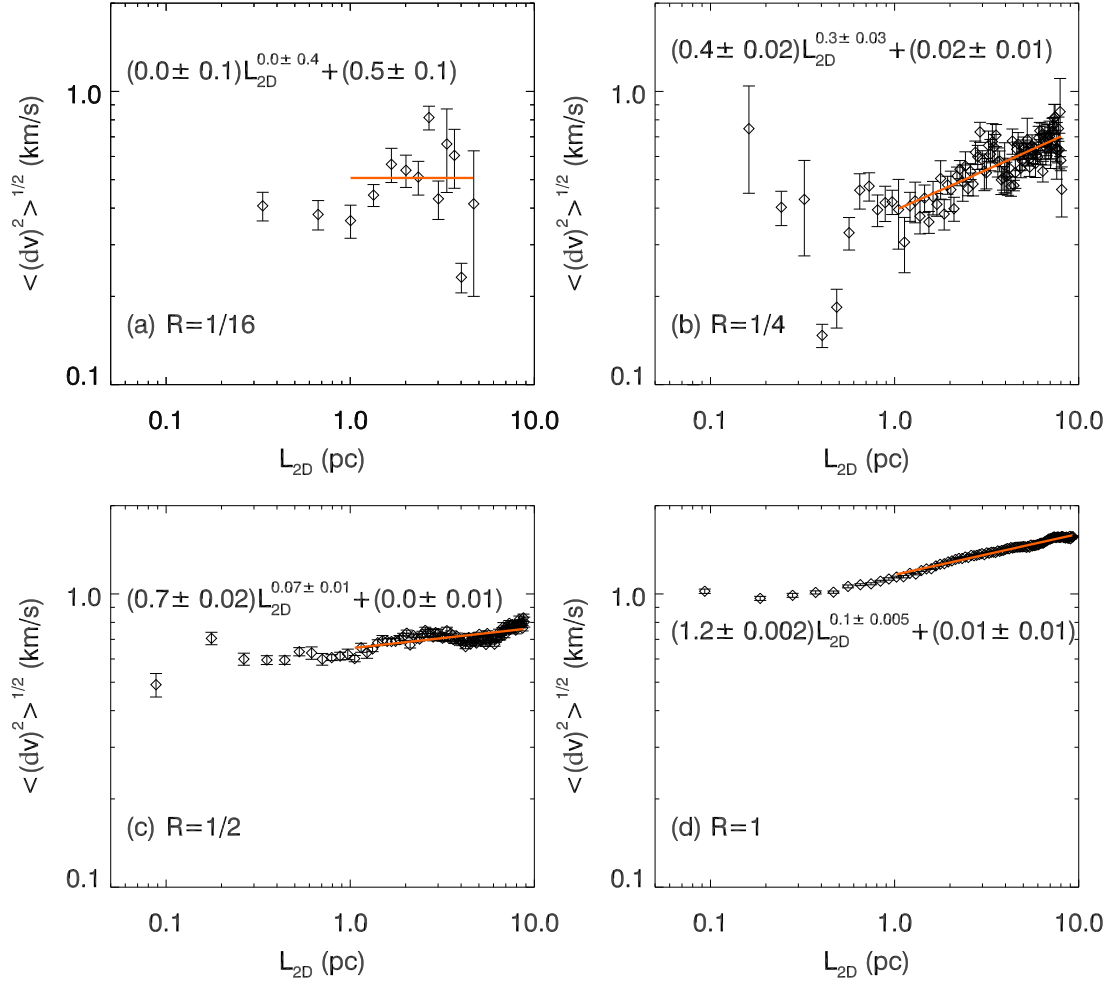


**Figure 16.** The CVD plot for a simulated cloud with a line of sight thickness of (a) 0.625 pc (with  $\mathcal{R} = 1/16$ ); (b) 2.5 pc (with  $\mathcal{R} = 1/4$ ); (c) 5 pc (with  $\mathcal{R} = 1/2$ ); (d) 10 pc (with  $\mathcal{R} = 1$ ). For all panels, the Mach number is 14. The fitting range is 1 pc to 10 pc, corresponding to the flat part of the energy spectrum of the hydrodynamical simulation (see figure 2).